Morphology, Crystal Structure and Charge Transport in Donor–Acceptor Block Copolymer Thin Films

Gaurav Gupta,[†] Chetan R. Singh,[‡] Ruth H. Lohwasser,[§] Marcel Himmerlich,[‡] Stefan Krischok,[‡] Peter Müller-Buschbaum,[⊥] Mukundan Thelakkat,[§] Harald Hoppe,[‡] and Thomas Thurn-Albrecht*,[†]

[†]Institut für Physik, Martin-Luther-Universität Halle-Wittenberg, von-Danckelman Platz 3, 06120 Halle (Saale), Germany
[‡]Institut für Physik, Technische Universität Ilmenau, 98693 Ilmenau, Germany
[§]Makromolekulare Chemie I, Universität Bayreuth, 95440 Bayreuth, Germany, and
[⊥]Physik-Department, Lehrstuhl für Funktionelle Materialien, Technische Universität München, James-Franck-Strasse 1, 85748 Garching, Germany

S Supporting Information
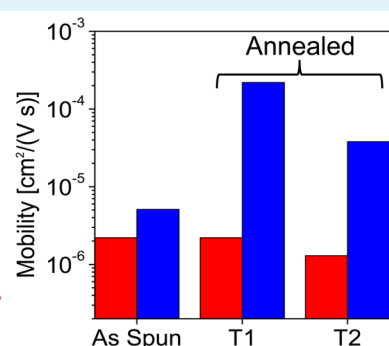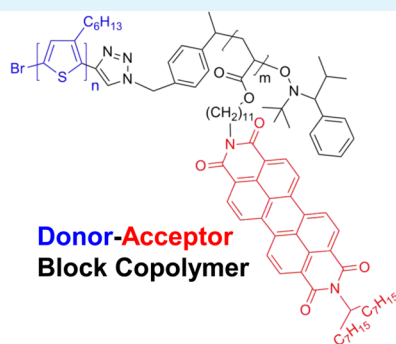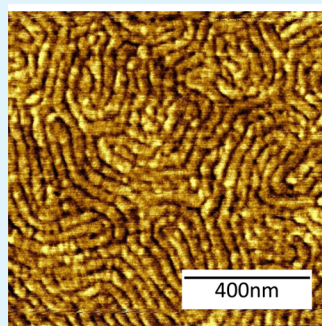
ABSTRACT: We studied structure and charge transport properties of thin films of donor–acceptor block copolymers, poly(3-hexylthiophene-*block*-perylene bisimide acrylate), using a combination of X-ray scattering, AFM and vertical charge transport measurements in diode devices. Block copolymer self-assembly and crystallization of the individual components are interrelated and different structural states of the films could be prepared by varying preparation conditions and thermal history. Generally the well-defined microphase structures found previously in bulk could also be prepared in thin films, in addition alignment induced by interfacial interactions was observed. Microphase separated block copolymers sustain ambipolar charge transport, but the exact values of electron and hole mobilities depend strongly on orientation and connectivity of the microdomains as well as the molecular order within the domains.

KEYWORDS: donor–acceptor block copolymers, thin films, microphase structure, crystal texture, X-ray scattering, charge carrier mobility

1. INTRODUCTION

The use of conjugated polymers in organic electronics, in particular in photovoltaic devices, has become an intense field of research during the past few years. Devices based on organic materials offer potential advantages in terms of solution processability, application to large areas, and fabrication on flexible substrates.[1,2] Despite significant advances and steadily increasing efficiencies in organic photovoltaics,[3] control of morphology and long-term morphological stability is an issue in polymer based bulk heterojunction devices obtained by blending donor and acceptor components. The control of morphology in such bulk heterojunction devices is limited due to the nonequilibrium nature of the demixing process. Device performance is generally strongly influenced by processing history and thermal or solvent treatment.[4−7] A different approach toward achieving a controlled morphology is the use of block copolymers consisting of covalently linked donor

and acceptor blocks. With such materials, the self-assembling properties of block copolymers can be utilized to prepare a well-defined and stable donor–acceptor nanostructure.[8] After some initial studies by Hadziioannou et al. and Thelakkat et al.[9,10] based on amorphous blocks later mostly block copolymers containing poly(3-hexylthiophene) (P3HT) as a donor block were synthesized.[11−20] In most cases though, either no clear evidence of a well-defined nanostructure was seen, or the nanostructure formation was driven by the crystallization of P3HT as e.g. shown explicitly by Verduzco et

al.[19] As a consequence, mostly elongated fibrils or lamellar structures of P3HT were observed instead of microphase separated structures. Some evidence for nanostructures based on conventional microphase separations were shown by Guo et al.[21] and Ku et al.[22] Recently we demonstrated detailed evidence for microphase separation in the melt and subsequent confined crystallization in a number of poly(3-hexylthiophene)-*block*-poly(perylene bisimide acrylate) (P3HT-*b*-PPerAcr) block copolymer systems in bulk samples.[23] These materials show well-defined lamellar and cylindrical microphase structures consisting of crystalline-liquid crystalline donor and acceptor microdomains, respectively. The morphology is controlled by molecular weight and volume fraction of the two blocks as it is well-established for liquid—liquid microphase separation. In this publication we present as a next step a combined study of the morphology and crystalline order of these materials in thin films together with transport measurements in diode device structure. Briefly, we show that the microstructural order (lamellar/cylindrical) observed in bulk samples is preserved in thin films. Because of interaction with the substrate and the surface, the microdomains orient parallel to the substrate in annealed films. Besides microstructural order, thermally annealed films exhibit an enhanced crystalline order and texture. The charge transport properties are strongly dependent on the alignment as well as on the amount of crystalline order and the donor—acceptor nanostructure.

2. EXPERIMENTAL SECTION

2.1. Samples and Sample Preparation. Figure 1 shows the chemical structure of the donor—acceptor block copolymers used for
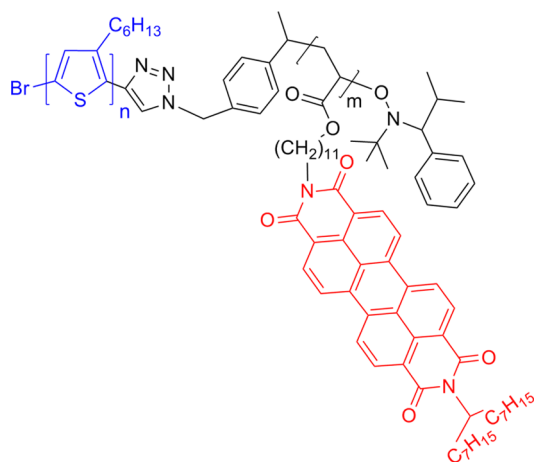

Figure 1. Chemical structure of the investigated block copolymer P3HT-*b*-PPerAcr (BCP C and BCP L). The first block consists of donor poly(3-hexylthiophene) (P3HT) (blue) and the second block is built of a flexible polyacrylate backbone with pendant side chains of perylene bisimides (red).

this study. Synthesis and self-assembly properties in bulk of the two materials studied, BCP C (P3HT-*b*-PPerAcr 6) and BCP L (P3HT-*b*-PPerAcr 5), were described elsewhere.[23] The molecular weight and composition of the samples is shown in Table 1. For size exclusion chromatography (SEC), polystyrene was used as an standard. For structural investigations, thin films of BCP C and BCP L were spin-coated from chloroform (14 mg/mL, 1000 rpm for 60 s) on Si wafers cleaned beforehand with sulfuric acid. The films were dried in vacuum at room temperature for several hours and subsequently subjected to different thermal treatments. Based on DSC results, films from both block copolymers were either annealed for 10 min above the respective

Table 1. Material Properties of BCP C and BCP L as Determined by SEC, MALDI-TOF MS, ^{1}H-NMR^a

	M_n (SEC) (kg/mol)	PDI	repeating units P3HT (MALDI-TOF MS)/ PPerAcr (^{1}H NMR)	wt % PPerAcr (^{1}H NMR)	volume fraction $\phi_{PPerAcr}$
BCP C	35.5	1.19	75/27	64	0.61
BCP L	28.4	1.13	75/13	47	0.44

^{a}The volume fraction of PPerAcr was estimated using the weight fraction (as obtained from ^{1}H-NMR) and the crystallographic density.

melting temperature of the PPerAcr component (215° for BCP C and 205 °C for BCP L; referred to as annealed in state T1) and subsequently cooled, or were heated to 250 °C above the melting temperature of the P3HT component for 10 min (referred to as annealed in state T2) and then cooled to room temperature. The heating and cooling rate was set at 10 °C/min on a Linkam hot stage, all steps were performed in nitrogen atmosphere. The film thicknesses were measured by AFM ($d \approx 180$ nm for BCP L and $d \approx 140$ nm BCP C). For SCLC measurements different substrates were used as described below and the same thermal treatment was applied. AFM test measurements performed on films of BCP C on PEDOT:PSS showed no effect of the substrate on the morphology of block copolymer films (see the Supporting Information, Figure 11).

2.2. Experimental Methods and Instrumentation. *2.2.1. DSC.* Differential scanning calorimetry (DSC) measurements on bulk samples were performed on a PerkinElmer DSC 7 with a heating/cooling rate of 10 °C/min. The first heating run was not considered. Background signals were subtracted for calculating the apparent heat capacity $c_p(T)$.

2.2.2. Atomic Force Microscopy (AFM). AFM measurements were performed with a Nano Wizard I from JPK Instruments. All measurements were done in the intermittent contact mode using single crystal Si N-type cantilever tips from NT-MDT having a resonant frequency between (240 to 440) kHz with a force constant of (22 to 100) N/m. The operating frequency was kept at $\omega_{op} = 0.995 \, \omega_o$ and the amplitude set-point at a ratio of 0.8 with respect to the free amplitude. The phase difference was set to zero at operating frequency in absence of tip—sample interaction.

2.2.3. Grazing Incidence Scattering. Grazing incidence wide-angle X-ray scattering experiments (GIWAXS) were performed at beamline ID 10 at the ESRF, Grenoble complemented by additional GIWAXS and GISAXS (grazing incidence small-angle X-ray scattering) measurements at the beamline BW4 at HASYLAB. The wavelength of the X-ray beam at ESRF was 0.155 nm (0.138 nm at BW4). In both cases the beam was collimated using an assembly of slits, a horizontal and vertically focusing mirror assembly in combination with Beryllium refractive lens system resulting in a small beam size of 300 μm × 15 μm (36 μm × 18 μm at BW4) at the sample position. Additional motorized guard slits were used in order to enhance signal-to-noise ratio. For GISAXS an angle of incidence of 0.35° and for GIWAXS of 0.17° (0.2° at BW4) was used. 2D scattering patterns were collected using a PILATUS 3 M detector with 487 pixels x 619 pixels and a pixel size of 172 μm (MarCCD 165 with 2048 pixels x 2048 pixels with a pixel size of 79 μm at BW4). For GISAXS measurements the sample to detector distance was set to 2.08 m while for GIWAXS it was set to 29.2 cm (10.3 cm at BW4). The schematic of the GIWAXS geometry can be found in the Supporting Information (Figure 5).

2.2.4. X-ray Photon Spectroscopy (XPS). XPS and UPS measurements were performed under ultrahigh vacuum (UHV) conditions employing monochromated Al K_α and ultraviolet He II radiation as described in detail in ref.[24] Thin films of both block copolymers with a thickness of ~100 nm as well as P3HT and PPerAcr homopolymer reference films were spin coated onto glass substrates covered with a conducting ITO layer. To avoid surface modification due to contact with the air, all samples were transferred in a HV transfer system (base pressure 1×10^{-6} mbar) filled with inert gas from the glovebox to the XPS and UPS system.

2.2.5. UV–Vis Absorption Spectroscopy. Measurements were carried out using a Varian Cary 5000 spectrophotometer. Thin films for UV–vis absorption measurements were prepared on glass substrates by spin coating for both block copolymers. The film thickness was ~100 nm. Neglecting the reflection from film surfaces, the absorbance for the films was calculated as the negative logarithm of the transmitted to the incident radiation. Additionally the absorbance spectra for the pure homopolymer films (as-spun) having similar film thickness were measured.

2.2.6. Photoluminescence Spectroscopy(PL). PL was recorded with an Avantes avaspec 2048 fiber spectrometer PL setup using a 407 nm GaN semiconductor laser for excitation. Thin films of both block copolymers were spin coated on glass substrates having a film thickness of ~100 nm.

2.2.7. Single Carrier Space Charge Limited Current Devices (SCLC). Single-carrier SCLC devices in diode configuration were prepared for charge carrier mobility determination of holes and electrons within the layer stack of glass/ITO/PEDOT:PSS/Active layer/Au and glass/PEDOT:PSS/Al/Active layer/Ca/Al, respectively. A schematic of the SCLC device is shown in the Supporting Information (Figure 9). For hole only devices, ITO coated glass substrates were etched at the region of contact to the Au and subsequently cleaned in toluene, acetone, and isopropanol. A layer of PEDOT:PSS (30 nm) was spin-coated onto the substrates in both types of devices for different purposes. In hole-only devices it provided ohmic contact for hole injection into the active layer. In electron-only devices, it was used to planarize the rough glass substrates. After depositing the bottom electrodes (PEDOT:PSS or 100 nm thick aluminum under high vacuum conditions), polymer solutions were spin-cast (20 mg/mL in chloroform, 450 rpm) on top of the bottom electrode under inert conditions resulting in film thicknesses in the range of 250 to 400 nm. Subsequently the films were thermally treated as described above and then slowly cooled (10 °C/min) to room temperature. The top electrodes (Au and Ca/Al) electrodes were thermally evaporated onto the polymer layer in respective devices under high vacuum conditions. The devices were encapsulated using glass and an epoxy resin under inert environment and characterized in the dark at room temperature with a Keithley 2400 source measure unit.

The charge carrier mobilities were evaluated by fitting measured J–V characteristics in a voltage range from 2 to 6 V using the Mott–Gurney law, cf. eq 1.[25] Thereby both the built-in voltage (V_{bi}) and the voltage drop (IR) over the series resistance were subtracted prior to fitting the measured J–V characteristics (J, current density; I, current). For this purpose the series resistances were determined from reference devices fabricated without active layers and were found to be 5.3 Ω and 2.5 Ω for the hole-only respectively electron-only devices. Because of the similar values of the work function for the two electrodes in hole-only devices and an expected Fermi level pinning of the Ca electrode to the LUMO level of the PPerAcr material in electron-only devices,[26] only a small the value of V_{bi} was to be expected, even for the electron-only devices. For the analysis, a V_{bi} in the range 0 to 0.4 V was tested. The value that provided minimum deviation between measured and fitted curve was selected.

3. RESULTS AND DISCUSSION

3.1. Thermal Properties. Table 2 summarizes the thermal and structural properties of the block copolymers investigated in this study. Detailed analysis of the bulk properties of BCP C

Table 2. Thermal Properties and Microphase Morphology of BCP C and BCP L in Bulk Samples As Determined by Differential Scanning Calorimetry and X-ray Scattering

	T_m (°C)	T_c (°C)	microphase morphology (periodicity)
BCP C	213/232/246	190/177	hexagonal (49 nm)
BCP L	193/228/239	180	lamellar (42 nm)

and BCP L have been described by Lohwasser et al.[23] Although P3HT is a well-known semicrystalline[27] polymer, PPerAcr orders in a liquid crystalline phase.[28] For simplicity, these two ordering processes will be summarized in the following under the term crystallization. SAXS studies on bulk samples revealed that both copolymers, BCP C and BCP L, are microphase separated at high temperatures above the melting point of the two components. BCP L forms a lamellar and BCP C a cylindrical microstructure which is retained upon cooling to room temperature as observed by SAXS and TEM (confined crystallization). The crystalline structure of the components are the same as observed in the corresponding homopolymers. The DSC heating curves of both materials as shown in Figure 2
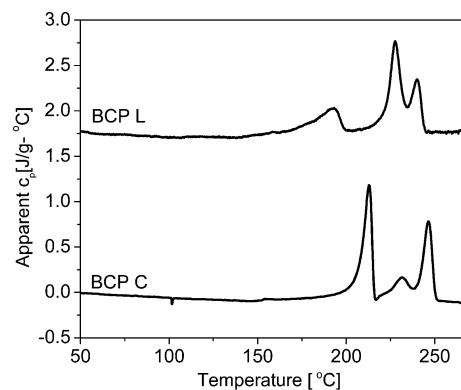

Figure 2. DSC heating curves of BCP C and BCP L measured with a scan rate of 10 °C/min.

exhibit three melting peaks. Although the first peak can be attributed to the melting of PPerAcr block, the peaks at higher temperatures can be ascribed to the melting of the P3HT block. Based on the DSC results, three thermodynamic states with respect to crystallization could be identified namely, (i) the low-temperature state where both the components are crystalline ($T < T_{mPPerAcr} < T_{mP3HT}$), (ii) intermediate-temperature state $T1$ where the P3HT is crystalline while PPerAcr is in molten phase ($T_{mPPerAcr} < T1 < T_{mP3HT}$); and (iii) the high-temperature state $T2$ where both the components are liquid like ($T_{mPPerAcr} < T_{mP3HT} < T2$). Crystallization of both blocks during cooling occurs either simultaneously (BCP L) or over a very narrow temperature range (BCP C). From a detailed analysis of the DSC melting enthalpies we could show that the crystallinity within the blocks is similar as in the corresponding homopolymers, indicating that the block copolymer morphology does not suppress crystallization.[23] On the basis of this knowledge, we here studied whether the microphase morphology and crystalline order, as observed in the bulk, persists in thin films and second, what is the relation between the microstructural, crystalline order, and orientation on the transport properties. For this purpose, we analyzed three sets of films, prepared analogously for both materials. The first set of films was as obtained directly from spin coating. The structure in as spun films corresponds to a trapped non-equilibrium state possessing neither microphases nor crystalline order. Heating these films to temperatures above the melting point of PPerAcr ($T = 215$ °C for BCP C and $T = 205$ °C for BCP L), annealing for 10 min and subsequent cooling leads to crystallization of both components without formation of a well developed microphase separated structure. The third set of films was heated to $T = 250$ °C, i.e., above the melting point of

both PPerAcr and P3HT, annealed there for 10 min, and subsequently cooled. As we will show, this treatment leads to the formation of well-developed microphase separated structure besides crystalline order. The former treatment will be termed as annealed in state $T1$, whereas the latter treatment will be referred as annealed in state $T2$.

3.2. Microphase Morphology. Figure 3 shows AFM height images of block copolymer thin films of BCP C and BCP
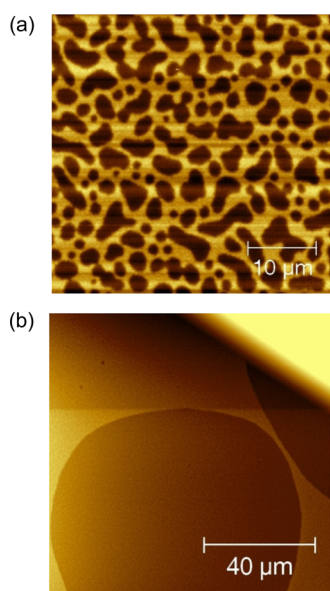

Figure 3. AFM height images of block copolymer films annealed in state $T2$ ($T_{mPPerAcr} < T_{mP3HT} < T2$) exhibiting islands and holes: (a) BCP C (scan area 40 μm × 40 μm) and (b) BCP L (scan area 100 μm × 100 μm).

L annealed in state $T2$. Both samples exhibit a morphology of islands and holes typical for block copolymers in thin films. The presence of such relief features is an indication for a microphase separated state with microdomains orientated parallel to the substrate.[29−31] The formation of such structures is a consequence of the mismatch between the film thickness and the periodicity of the microstructure. Profile scans across such structures give step heights of ~40 nm (BCP L) and ~45 nm (BCP C) which is in agreement with the corresponding bulk periodicity values as obtained from SAXS.[23] Images obtained from optical microscopy of BCP L (see the Supporting Information, Figure 2) confirm the presence of large islands and holes in line with the AFM measurements.

Materials contrast can be observed using the phase image information on AFM measurements.[32] Figure 4 shows such phase images of BCP C and BCP L from a smaller scan area for the as-spun and thermally treated films. As usual, the as-spun films show no special structure as the state after spin coating corresponds to a more or less homogeneous nonequilibrium state trapped by the fast drying process. On the other hand, the film of BCP C annealed in state $T2$ exhibits flat lying cylindrical microstructures indicating well-defined microdomains. The fact that no microstructures were observed for BCP L annealed in state $T2$ is consistent with lamellar microdomains lying parallel to the substrate. Note that the film of BCP C annealed in state $T1$ shows no cylindrical structures indicating that annealing below the melting temperature of P3HT is not sufficient for the development of a well-defined microphase structure. Presumably it is suppressed by the fast crystallization of P3HT from the quenched amorphous state, which fixes an only locally demixed state.

To gain a more detailed insight into the wetting behavior, thickness measurements and XPS experiments were performed on films of BCP L (lamellar microdomains) annealed in state $T2$. The parallel orientation above-mentioned is caused by the
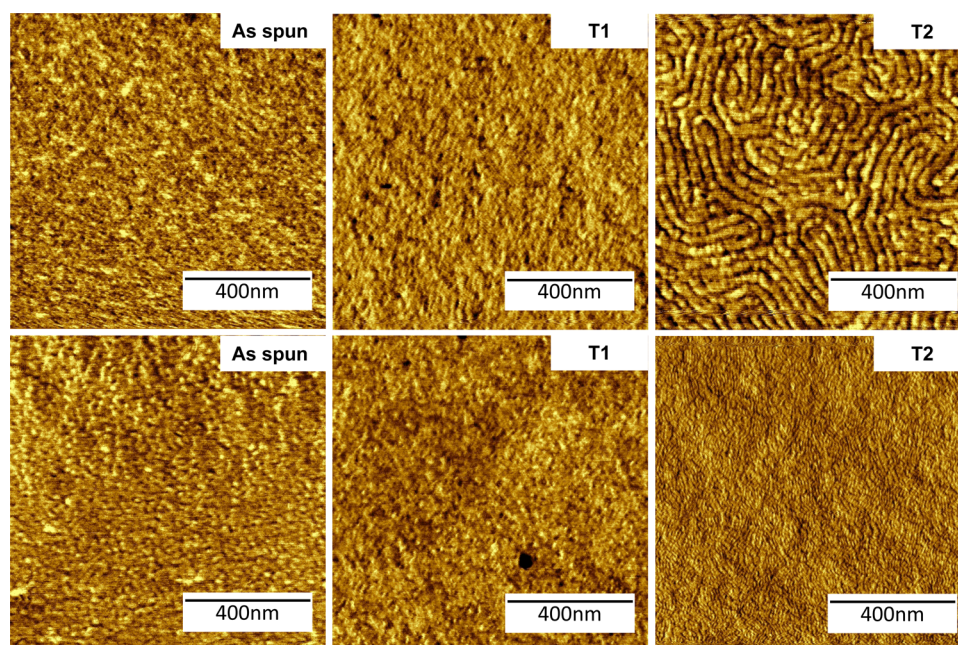

Figure 4. AFM phase images of as spun and annealed films of BCP C (top) and BCP L (bottom); no microphase separation is observed in as spun and films annealed in state $T1$ ($T_{mPPerAcr} < T1 < T_{mP3HT}$). Whereas flat lying cylindrical microstructures are observed in BCP C films annealed in state $T2$ ($T_{mPPerAcr} < T_{mP3HT} < T2$), no microstructures are observed in BCP L films annealed in state $T2$, consistent with parallel orientation of lamellar microdomains. The images are scanned over film area of 1 μm × 1 μm.

interaction of the two components with the surfaces.[33,34] The quantization rule for stable film thickness for symmetric and asymmetric wetting for a lamellar microstructure oriented parallel to substrate is given by $d = nL$ and $d = (n + 1/2)L$, respectively, where n is an integer and L the period of the microstructure.[34] The film thickness as measured by AFM and X-ray reflectivity measurements (not shown here), was found to be ~180 nm which corresponds to the quantization rule for the case of asymmetric wetting with $n = 4$, implying that different components wet the substrate/air interface.

XPS measurements, presented in the Supporting Information (Figure 1a), show enhanced oxygen and nitrogen signals and a simultaneous decrease of that of sulfur at the surface for films which were annealed in state $T2$ as compared to the as spun (nonmicrophase separated) films. Moreover, the corresponding UPS valence band spectrum of BCP L annealed in state $T2$ (Supporting Information, Figure 1b) is in very good agreement with the reference fingerprint spectrum of PPerAcr, while the spectral dependence of the as spun BCP L films resembles a superposition of P3HT and PPerAcr according to their copolymer molecular structure, revealing the unordered distribution of the diblock copolymer units at the surface of nonthermally treated films. These experimental results clearly indicate the presence of a PPerAcr layer at the polymer film surface after annealing of BCP in state $T2$. Although the thickness of the films used for XPS and UPS measurements was 100 nm, the quantization rule for stable film thickness would be the same, i.e. asymmetric wetting (with $n = 2$). Thus, in the lamellar microphase separated films of BCP L, P3HT wets the substrate and PPerAcr wets the surface.

Because AFM probes only the surface morphology of thin films, the internal microstructure was investigated using GISAXS. Figure 5 shows the 2D GISAXS pattern of BCP C
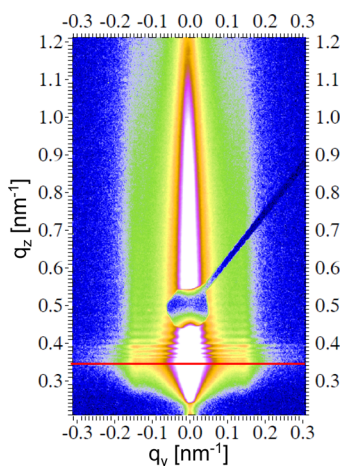
Figure 5. 2D GISAXS image of a thin film of BCP C annealed in state $T2$ ($T_{mPPerAcr} < T_{mP3HT} < T2$). The specular reflection is masked by a beam stop. The red line indicates the Yoneda position at which horizontal line cuts were taken.

films annealed in state $T2$ as a reciprocal space map. The small q_x component (along the direction of incident beam) was neglected as in GISAXS geometry all angles are small. The corresponding transformation equations used for data conversion are given in ref 35. Scattering patterns of the as spun films and films annealed in state $T1$ can be found in the Supporting Information (Figures 3 and 4). Only films of BCP C annealed in state T2 exhibit maxima in intensity along the q_y

axis at $q_y = 0.14$ nm^{-1} around the Yoneda position ($\alpha_f = \alpha_c$), implying a laterally periodic microdomain structure in the film. Figure 6a shows the corresponding horizontal line cut of the
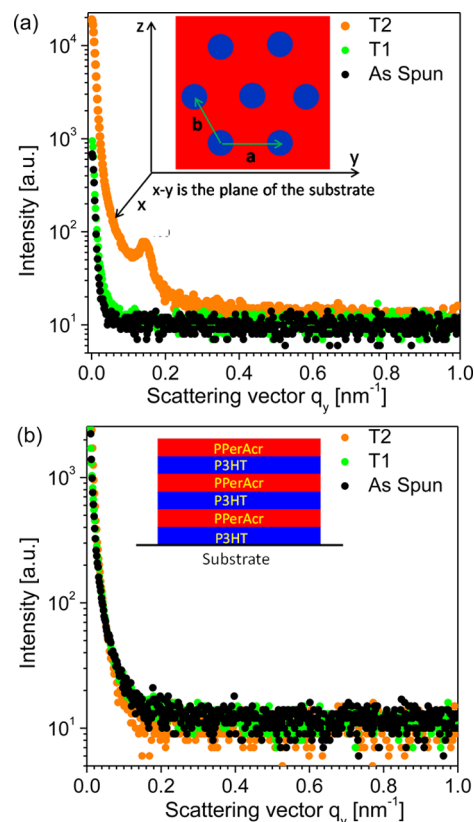
Figure 6. Horizontal line cut at the Yoneda position of the 2D GISAXS data of as spun and thermally treated (annealed in state $T1$: $T_{mPPerAcr} < T1 < T_{mP3HT}$; and state $T2$: $T_{mPPerAcr} < T_{mP3HT} < T2$) films of (a) BCP C and (b) BCP L. The insets show a schematic of the suggested orientation of the microdomain structure.

2D GISAXS pattern at $\alpha_f = \alpha_c$ for films with different thermal treatments. The periodicity of the microstructure corresponding to this maximum in the intensity is $2\pi/q_y = 45$ nm, which compares reasonably well with the periodicity of the cylindrical microphase structure of 49 nm found in bulk samples.[23] The appearance of the peak in the scattering signal is also consistent with the AFM image in Figure 4 showing cylindrical microdomains in the plane of the substrate. The fact that the GISAXS data of BCP L show no peak (cf. Figure 6b) is in line with the absence of well-defined microdomains for the state after spin coating and after annealing in state $T1$ and also consistent with the suggested lamellar microdomains parallel to the substrate for samples annealed in state $T2$. A possible peak on the q_z-axis reflecting the vertical microstructure was generally not observed, most likely due to the small density contrast at the internal interfaces in comparison to the outer interfaces to air and substrate. A schematic of the proposed microstructures is shown in the insets of Figure 6.

3.3. Crystal Texture. The crystalline order and texture in thin films was investigated using GIWAXS. The scattering signal of as spun films (Supporting Information, Figure 7) exhibited a diffuse scattering pattern without Bragg reflections corresponding to a quenched/amorphous state. Figure 7 shows the scattering patterns of films annealed in state $T1$ and $T2$. In
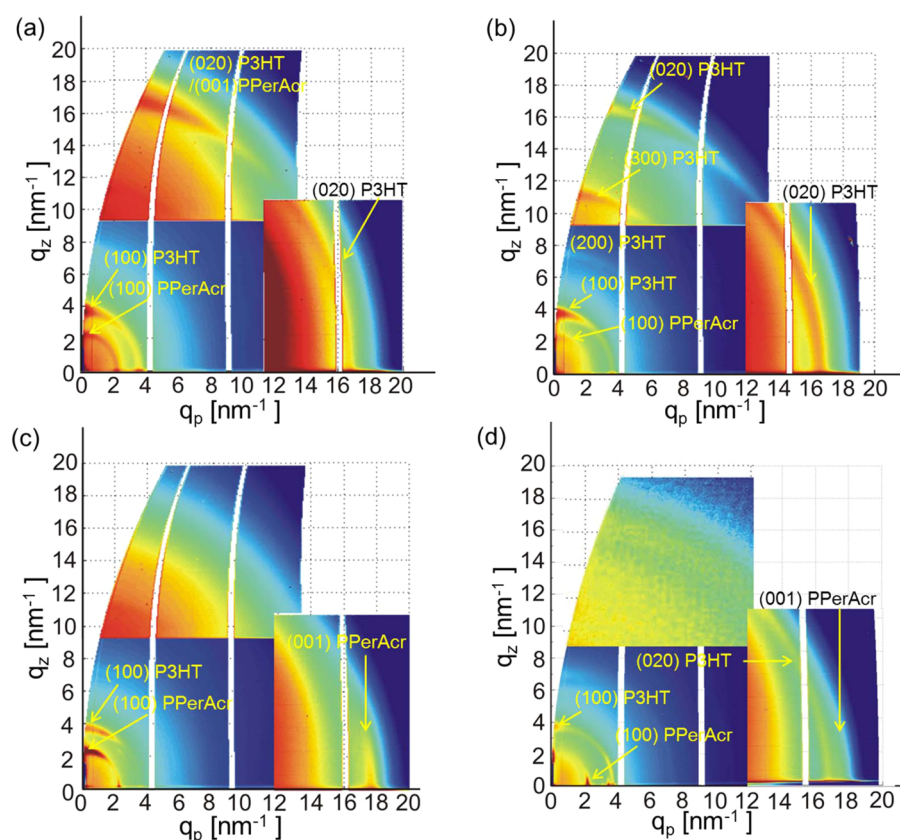
Figure 7. 2D GIWAXS reciprocal space maps of thin films of (a, c) BCP C and (b, d) BCP L. (a, b) Space maps of films annealed in state $T1$ ($T_{mPPerAcr} < T1 < T_{mP3HT}$), and (c, d) films annealed in state $T2$ ($T_{mPPerAcr} < T_{mP3HT} < T2$). The color (log) scale in each region of measurement is different and chosen such that the reflections are well visible. The same color scale is kept for the same region for the different thermally treated films. Bragg reflections from the respective components, i.e., P3HT and PPerAcr, are indicated with arrows.

both cases, distinct Bragg reflections indicate crystalline order. The reflections are located at the same scattering vector positions as in the respective homopolymers. Besides showing crystalline order, the GIWAXS patterns give indication of a strong crystalline texture. Before starting the analysis, let us recall that as homopolymers both blocks show an edge-on orientation in thin films with the (100) reflection on q_z-axis (cf. Supporting Information, Figure 6, for P3HT and ref 28 for PPerAcr). Generally, for the films annealed in state $T1$, crystallization of P3HT either occurs during the heating or annealing which hinders the formation of any long-range microstructural order; PPerAcr crystallizes subsequently during cooling. On the other hand, in the films annealed in state $T2$ crystallization occurs during cooling after formation of a well-defined microphase structure in the melt state. We first discuss the crystalline texture in films annealed in state $T1$ beginning with the BCP C sample containing cylindrical microdomains. Bragg reflections (100) from PPerAcr and P3HT show intensity distributed over the entire azimuthal angular range (meridional to equatorial position) with intensity maxima close to the q_z (meridional) and q_p (equatorial) axis. Correspondingly one would expect that the (020) of P3HT and the (001) of PPerAcr, both corresponding to the $\pi-\pi$ stacking, also exhibit maxima at the same azimuthal positions. But, as these latter reflections are broad and therefore difficult to resolve only the maximum close to the meridian is clearly visible. For the equatorial position the reflections are in addition close to the detector edge. A similar orientation distribution was observed for sample BCP L containing lamellar microdomains, although

the maxima close to the q_z axis are more dominant in this case. Also, due to the smaller PPerAcr content in this block copolymer, the (020) of P3HT dominates while the (001) of PPerAcr is too weak to be observed. All together, the films show an anisotropic texture that is different from the texture observed for the homopolymers and without one single preferred crystalline orientation.

Let us now analyze the crystalline texture for the films annealed in state $T2$. Generally, the observed scattering patterns are similar to what was discussed before, showing maxima of the dominant (100) reflections on the meridian and on the equator. However, as a general feature the reflections are more narrow, indicating larger crystalline domains and in most cases the orientation seems better defined. For BCP C both blocks show a dominant but broadly distributed orientation with the (100) reflection on the meridian, i.e. the a-axis is approximately perpendicular to the substrate. The other component of the orientation distribution ((100) on the q_p axis) is weaker and only visible for the majority component PPerAcr. The observed strong orientation of the PPerAcr block, similar as in the case of PPerAcr homopolymer,[28] is to be expected in this sample, as PPerAcr forms a continuous phase. Previous temperature dependent scattering experiments indicated that during cooling of BCP C the PPerAcr block crystallizes first,[23] which would suggest that the observed anisotropic orientation of the P3HT crystals is a consequence of the orientation of the PPerAcr crystals, as both are coupled across the microdomain interfaces by the block copolymer chains.
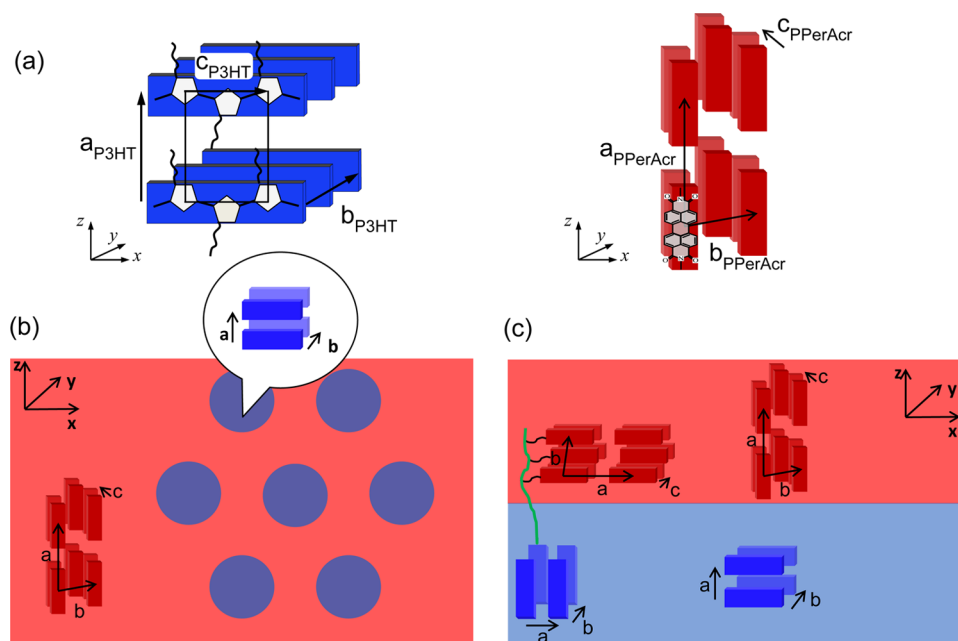
Figure 8. (a) Schematic of the crystal unit cell of P3HT and PPerAcr as observed in homopolymers. (b, c) Microstructural and crystalline order and orientation in thin films annealed in state T2 for (b) BCP C and (c) BCP L. Cylindrical and lamellar microdomains are lying flat within the thin film. In addition the preferred orientations of the crystal lattices are shown. Whereas for (b) BCP C, the orientation with *a*-axis perpendicular to the substrate is dominant, for (c) BCP L, both orientations are found with similar intensity, namely crystals with *a*-axis perpendicular to the substrate and crystals with *a*-axis parallel to the substrate.

The texture in films of the BCP L on the other hand is quite different and obviously strongly influenced by the microphase structure, which consists in this case of lamellae parallel to the substrate. The (100) reflections of PPerAcr and P3HT both exhibit a strong maximum on the q_p axis in addition to the signal on the q_z axis (Figure 7d). Consequently, both components have a mixed orientation distribution. Obviously, the microphase structure disturbs the orientation preferred by the substrate and interface and causes a component with the *a*-axis parallel to the substrate, consistent with a perpendicular orientation of the chains caused by the strongly oriented lamellar microphase structure.

In conclusion, the texture in the crystalline/liquid-crystalline block copolymer P3HT-*b*-PPerAcr is strongly affected by confinement effects in films having long-range microstructural order. Figure 8 gives a schematic overview of the observed structures.

3.4. Optical Properties. The absorbance and photoluminescence (PL) spectra of the as spun and thermally treated films of BCP C are shown in Figure 9a, b, respectively. For comparison, the absorbance spectra of pure homopolymer as spun films are also shown in Figure 9a. Both P3HT and PPerAcr absorb light in the visible spectrum, the absorption spectrum in the block copolymer films results from a superposition of the absorption in the individual phases. Comparing the absorbance spectra of BCP C films, the red-shift and the appearance of a vibronic peak at 615 nm[36] for the thermally treated films in comparison to as spun films highlight the increase in overall crystallinity and order after thermal treatment. Generally, the structured low energy band in the P3HT absorption spectrum is associated with planar chains that form weakly interacting H-aggregates.[36,37]

In the PL spectra, the highly quenched PL signal for the case of as spun BCP C film demonstrates a disordered morphology and a minimum scale of phase separation between donor and
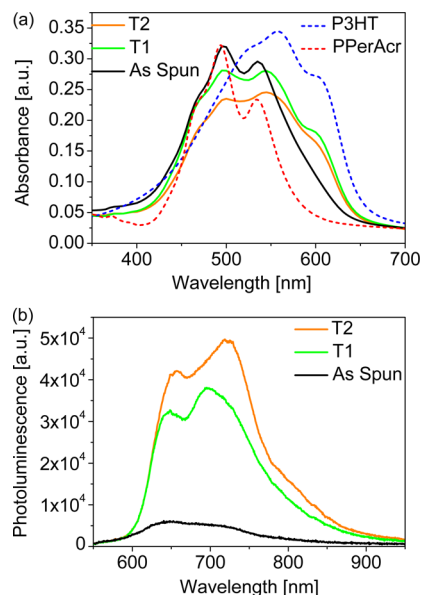

Figure 9. (a) Thin film absorption spectra of the as spun, and thermally treated films of BCP C and corresponding homopolymer (as spun) films of similar thickness (b) Photoluminescence signal from the BCP C having same film thickness. The intensities of the absorbance and PL spectra can be compared within the individual methods as the film thickness of all the films were same.

acceptor components directly after spin coating. However, in the case of thermally treated films, higher PL efficiency (increase by an order of magnitude) was observed as compared to the as spun films, which demonstrates the formation of larger microdomains. Similar optical response and PL spectra (see the Supporting Information, Figure 8) were also observed for BCP

12315

dx.doi.org/10.1021/am5049948 | *ACS Appl. Mater. Interfaces* 2015, 7, 12309−12318

L films. These results are in agreement with the findings from structural investigations.

3.5. Charge Carrier Transport Properties. To study the effect of morphology on charge transport properties in BCP C and BCP L thin films, we determined both electron and hole mobilities by the method of space charge limited current (SCLC). The charge carrier mobilities in organic semiconductors are often determined by fitting measured $J-V$ characteristics by the empirical Murgatroyd formula.[38] However, compared to the simple Mott−Gurney law, the Murgatroyd formula uses two additional variables, namely, zero field mobility and field dependence parameter γ. The field dependence factor γ in the formula is generally very sensitive to disorder and to the series resistance of the substrate and therefore hard to determine in a consistent way for donor−acceptor devices with different morphologies.[39,40] Therefore, to compare the charge transport properties in a simple way, we used the Mott−Gurney law (eq 1) to determine an effective charge carrier mobility.[25]

$$J = \frac{9}{8}\epsilon_r\epsilon_0\mu\frac{V^2}{L^3} \qquad (1)$$

Here, J is the current density, ϵ_r the relative permittivity of the material (≈ 3.5), ϵ_0 the permittivity of vacuum, μ the charge carrier mobility, V the voltage across the active layer, and L the thickness of the active layer. For most $J-V$ curves, we observed a slope of 2 in the log J−log V plot in the voltage range between 2 and 6 V corresponding to the SCLC regime. For voltages below 2 V, we observed slopes less than 2 and we associate them with the ohmic region or transition between the ohmic and the SCLC region. Thus, the charge carrier mobility values were obtained by fitting the measured data by the Mott−Gurney equation in the voltage range between 2 and 6 V. The mobility values from each film were checked for reproducibility by repeating every experiment at least at twice. Representative data obtained for the as spun films of the block copolymers are shown in Figure 10. The corresponding $J-V$ characteristics for the thermally treated films for BCP C and BCP L can be found in the Supporting Information, Figure 10.

Figure 11 summarizes the charge carrier mobilities of holes and electrons obtained for films of BCP C and BCP L and
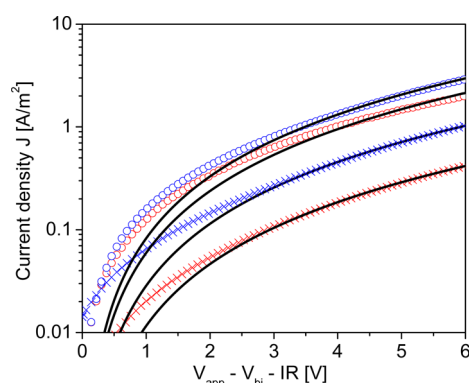

Figure 10. Exemplary $J-V$ characteristics of BCP L (open circles) and BCP C (crosses) as spun devices measured at room temperature in diode configuration. Blue and red symbols denote the $J-V$ characteristic for hole only and electron only devices, respectively. The solid black lines represent the SCLC fit according to eq 1. Note that the film used for measuring the hole mobility of BCP C had a somewhat larger thickness than the other three samples.

shows for comparison the mobilities obtained from pure homopolymer films. Already for the homopolymers the electron and hole mobilities of the quenched amorphous state after spin coating were about an order of magnitude lower than the mobilities in films that were crystallized by cooling from the melt. These findings are in agreement with previous results on the P3HT homopolymers.[41] The charge carrier mobility of electrons and holes in as spun block copolymers films (BCP C and BCP L) was further reduced by more than an order of magnitude. This result is consistent with the intermixed morphology without percolating pathways of pure donor and acceptor phases and is in line with the highly quenched PL signal for the as-spun block copolymer films. It is known that charge transport in blends is generally reduced and depends on the volume fraction and domain size.[42] The ratio of hole mobility to electron mobility in as spun BCP C film was similar to that in pure homopolymer films, i.e., the hole mobility was found to be an order of magnitude higher than the electron mobility. Upon annealing in state T1 and T2, a clear increase in both electron and hole mobility took place, showing a strong effect of microdomain size and purity on charge transport. But even after annealing in state T2, the electron mobility that is supposed to be supported by a continuous PPerAcr phase is considerably lower than in the corresponding homopolymer. Obviously loss of charge carriers due to the presence of donor material is high. It could possibly be further reduced by enlarging the size of PPerAcr microdomains.[43] For BCP L the effect of annealing is somewhat different, cf. Figure 11b. Annealing the films in the state T1 led only to an increase in the hole mobility. This sample lacks a continuous PPerAcr phase leading obviously to a stronger suppression of the electron mobility. It is interesting to note that annealing in state T2 resulted in a lower value for the hole mobility than annealing in state T1. Obviously the ordered microstructure of donor and acceptor lamellae parallel to the substrate opposes vertical transport. However, the hole mobility is still higher than in BCP C after annealing in state T2. Most likely the probability for structural defects leading to continuous pathways for hole transport between the electrodes is higher in BCP L than BCP C. The XPS/UPS measurements support this assumption. Even in BCP L after annealing in state T2, there is some remaining intensity from sulfur atoms visible (see the Supporting Information, Figure 1), which would be unexpected for a perfectly aligned lamellar morphology. All together, the results show that a block copolymer based donor−acceptor nanostructure can support ambipolar charge transport, but the electron and hole mobilities depend strongly on crystallinity, size, and connectivity of the microdomains. In addition, crystal orientation within the microdomains will certainly play a role. But as for the current system, we have no means to vary this quantity independently, it is difficult to make an estimate of its relative importance.

4. CONCLUSIONS

We investigated microstructure, crystalline order, and orientation in donor−acceptor block copolymers and measured electron and hole mobilities in devices containing materials with different morphology. The well-defined microphase structures which were found before for the same materials in bulk are preserved in thin films. Generally, the effect of the thin film geometry on self-assembly properties of the investigated donor−acceptor block copolymer is very similar to more simple systems studied in the past. Because of interfacial interaction,
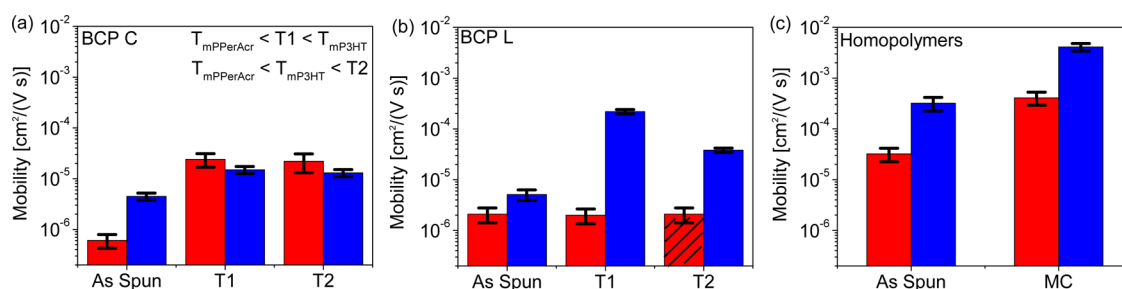
Figure 11. SCLC mobilities of electrons (red) and holes (blue) for as cast and thermally treated (annealed in state T1 and state T2) films of (a) BCP C and (b) BCP L. The error bars denote the corresponding error in the mobility values due to variation in measured film thickness. The electron mobilities in BCP L films annealed in state T2 (hatched column) are indicative only of the order of magnitude. (c) SCLC charge carrier mobilities in as cast and melt cooled films of pristine homopolymer (P3HT12 and PPerAcr) are shown for comparison. P3HT12[41] is the homopolymer with a molecular weight of 12.4 kg/mol (MALDI-TOF MS)) and has the same molecular weight as the P3HT block of the block copolymers used here.

microdomains tend to align parallel to the plane of the film. For the semiconducting materials, it is important to note that the crystallization of the individual components does not destroy the well-defined microphase structure. Similarly to blend morphologies, as they are used for organic solar cells, the charge carrier mobilities in the block copolymer materials are lower than in pure homopolymers and depend strongly on the orientation and connectivity of the microdomains as well as on the crystallinity within the microdomains. However, a potential advantage compared to blend materials is that the block copolymer architecture allows the preparation of a well-defined stable morphology with shape and size of the domains determined by the architecture and molecular weight of the polymer. An important further step toward usage of the investigated materials in solar cell devices will be to achieve vertical alignment of the microphase structure. The ability of one nanostructured material consisting of hole and electron conducting microdomains to support ambipolar charge transport, is in addition of potential interest for other devices as, for example, transistors.[16]

ASSOCIATED CONTENT

Ⓢ Supporting Information

Supplementary experimental results and supporting data. It includes XPS data, optical microscopy images, a sketch of the experimental setup for grazing incidence scattering experiments, GISAXS/GIWAXS scattering patterns, UV−vis absorbance and photoluminescence data, and results of SCLC measurements. This material is available free of charge via the Internet at http://pubs.acs.org/.

AUTHOR INFORMATION

Corresponding Author
*E-mail: thomas.thurn-albrecht@physik.uni-halle.de. Phone: +49-345-5525340. Fax: +49-345-5527160.

Notes
The authors declare no competing financial interest.

ACKNOWLEDGMENTS

REFERENCES

(1) Coakley, K.; McGehee, M. Conjugated Polymer Photovoltaic Cells. *Chem. Mater.* **2004**, *16*, 4533−4542.

(2) Brabec, C.; Hauch, J.; Schilinsky, P.; Waldauf, C. Production Aspects of Organic Photovoltaics and Their Impact on the Commercialization of Devices. *MRS Bull.* **2005**, *30*, 50−52.

(3) Green, M. A.; Emery, K.; Hishikawa, Y.; Warta, W.; Dunlop, E. D. Solar Cell Efficiency Tables (version 40). *Prog. Photovolt.: Res. Appl.* **2012**, *20*, 606−614.

(4) Erb, T.; Zhokhavets, U.; Gobsch, G.; Raleva, S.; Stühn, B.; Schilinsky, P.; Waldauf, C.; Brabec, C. Correlation between Structural and Optical Properties of Composite Polymer/Fullerene Films for Organic Solar Cells. *Adv. Funct. Mater.* **2005**, *15*, 1193−1196.

(5) Ma, W.; Yang, C.; Gong, X.; Lee, K.; Heeger, A. Thermally Stable, Efficient Polymer Solar Cells with Nanoscale Control of the Interpenetrating Network Morphology. *Adv. Funct. Mater.* **2005**, *15*, 1617−1622.

(6) Ruderer, M.; Müller-Buschbaum, P. Morphology of Polymer-Based Bulk Heterojunction Films for Organic Photovoltaics. *Soft Matter* **2011**, *7*, 5482−5493.

(7) Ruderer, M.; Guo, S.; Meier, R.; Chiang, H.; Krstgens, V.; Wiedersich, J.; Perlich, J.; Roth, S.; Müller-Buschbaum, P. Solvent-Induced Morphology in Polymer-Based Systems for Organic Photovoltaics. *Adv. Funct. Mater.* **2011**, *21*, 3382−3391.

(8) Robb, M. J.; Ku, S.-Y.; Hawker, C. J. 25th Anniversary Article: No Assembly Required: Recent Advances in Fully Conjugated Block Copolymers. *Adv. Mater.* **2013**, *25*, 5686−5700.

(9) de Boer, B.; Stalmach, U.; van Hutten, P.; Melzer, C.; Krasnikov, V.; Hadziioannou, G. Supramolecular Self-Assembly and Opto-Electronic Properties of Semiconducting Block Copolymers. *Polymer* **2001**, *42*, 9097−9109.

(10) Lindner, S.; Httner, S.; Chiche, A.; Thelakkat, M.; Krausch, G. Charge Separation at Self-Assembled Nanostructured Bulk Interface in Block Copolymers. *Angew. Chem., Int. Ed.* **2006**, *45*, 3364−3368.

(11) Sommer, M.; Lang, A.; Thelakkat, M. Crystalline-Crystalline Donor-Acceptor Block Copolymers. *Angew. Chem., Int. Ed.* **2008**, *47*, 7901−7904.

(12) Lee, J.; Cirpan, A.; Emrick, T.; Russell, T.; Jo, W. Synthesis and Photophysical Property of Well-Defined Donor-Acceptor Diblock Copolymer Based on Regioregular Poly(3-hexylthiophene) and Fullerene. *J. Mater. Chem.* **2009**, *19*, 1483−1489.

(13) Miyanishi, S.; Zhang, Y.; Keisuke, T.; Hashimoto, K. Fullerene Attached All-Semiconducting Diblock Copolymers for Stable Single-Component Polymer Solar Cells. *Chem. Commun.* **2010**, *46*, 6723−6725.

12317

dx.doi.org/10.1021/am5049948 | *ACS Appl. Mater. Interfaces* 2015, 7, 12309−12318

(14) Tao, Y.; McCulloch, B.; Kim, S.; Segalman, R. The Relationship Between Morphology and Performance of Donor-Acceptor Rod-Coil Block Copolymer Solar Cells. *Soft Matter* **2009**, *5*, 4219−4230.

(15) Zhang, Q.; Cirpan, A.; Russell, T.; Emrick, T. Donor-Acceptor Poly(thiophene-block-perylene diimide) Copolymers: Synthesis and Solar Cell Fabrication. *Macromolecules* **2009**, *42*, 1079−1082.

(16) Huettner, S.; Sommer, M.; Hodgkiss, J.; Kohn, P.; Thurn-Albrecht, T.; Friend, R.; Steiner, U.; Thelakkat, M. Tunable Charge Transport using Supramolecular Self-Assembly of Nanostructured Crystalline Block Copolymers. *ACS Nano* **2011**, *5*, 3506−3515.

(17) Tu, G.; Li, H.; Forster, M.; Heiderhoff, R.; Balk, L.; Scherf, U. Conjugated Triblock Copolymers Containing both Electron-Donor and Electron-Acceptor Blocks. *Macromolecules* **2006**, *39*, 4327−4331.

(18) Sommer, M.; Komber, H.; Huettner, S.; Mulherin, R.; Kohn, P.; Greenham, N.; Huck, W. Synthesis, Purification, and Characterization of Well-Defined All-Conjugated Diblock Copolymers PF8TBT-b-P3HT. *Macromolecules* **2012**, *45*, 4142−4151.

(19) Verduzco, R.; Botiz, I.; Pickel, D.; Kilbey, S.; Hong, K.; DiMasi, E.; Darling, S. Polythiophene-block-Polyfluorene and Polythiophene-block-Poly(fluorene-co-benzothiadiazole): Insights into the Self-Assembly of All-Conjugated Block Copolymers. *Macromolecules* **2011**, *44*, 530−539.

(20) Smith, K. A.; Pickel, D. L.; Yager, K.; Kisslinger, K.; Verduzco, R. Conjugated Block Copolymers via Functionalized Initiators and Click Chemistry. *J. Polym. Sci., Part A: Polym. Chem.* **2014**, *52*, 154−163.

(21) Guo, C.; Lin, Y.; Witman, M.; Smith, K.; Wang, C.; Hexemer, A.; Strzalka, J.; Gomez, E.; Verduzco, R. Conjugated Block Copolymer Photovoltaics with near 3% Efficiency through Microphase Separation. *Nano Lett.* **2013**, *13*, 2957−2963.

(22) Ku, S.; Brady, M.; Treat, N.; Cochran, J.; Robb, M.; Kramer, E.; Chabinyc, M.; Hawker, C. A Modular Strategy for Fully Conjugated Donor-Acceptor Block Copolymers. *J. Am. Chem. Soc.* **2012**, *134*, 16040−16046.

(23) Lohwasser, R.; Gupta, G.; Kohn, P.; Sommer, M.; Lang, A.; Thurn-Albrecht, T.; Thelakkat, M. Phase Separation in the Melt and Confined Crystallization as the Key to Well-Ordered Microphase Separated Donor-Acceptor Block Copolymers. *Macromolecules* **2013**, *46*, 4403−4410.

(24) Opitz, A.; Bronner, M.; Brütting, W. Electronic Properties of Organic Semiconductor Blends: Ambipolar Mixtures of Phthalocyanine and Fullerene. *Appl. Phys. Lett.* **2007**, *90*, 212112(1−3).

(25) Mott, N. F.; Gurney, R. W. *Electronic Processes in Ionic Crystals*; The Clarendon Press: Oxford, U.K., 1940.

(26) Braun, S.; Salaneck, W. R.; Fahlman, M. Energy-Level Alignment at Organic/Metal and Organic/Organic Interfaces. *Adv. Mater.* **2009**, *21*, 1450−1472.

(27) Wu, Z.; Petzold, A.; Henze, T.; Thurn-Albrecht, T.; Lohwasser, R.; Sommer, M.; Thelakkat, M. Temperature and Molecular Weight Dependent Hierarchical Equilibrium Structures in Semiconducting Poly(3-hexylthiophene). *Macromolecules* **2010**, *43*, 4646−4653.

(28) Kohn, P.; Ghazaryan, L.; Gupta, G.; Sommer, M.; Wicklein, A.; Thelakkat, M.; Thurn-Albrecht, T. Thermotropic Behavior, Packing, and Thin Film Structure of an Electron Accepting Side-Chain Polymer. *Macromolecules* **2012**, *45*, 5676−5683.

(29) Busch, P.; Posselt, D.; Smilgies, D.; Rheinlnder, B.; Kremer, F.; Papadakis, C. Lamellar Diblock Copolymer Thin Films Investigated by Tapping Mode Atomic Force Microscopy: Molar-mass Dependence of Surface Ordering. *Macromolecules* **2003**, *36*, 8717−8727.

(30) Kim, H.; Russell, T. Ordering in Thin Films of Asymmetric Diblock Copolymers. *J. Polym. Sci., Part B: Polym. Phys.* **2001**, *39*, 663−668.

(31) Ham, S.; Shin, C.; Kim, E.; Ryu, D.; Jeong, U.; Russell, T.; Hawker, C. Microdomain Orientation of PS-b-PMMA by Controlled Interfacial Interactions. *Macromolecules* **2008**, *41*, 6431−6437.

(32) Schroeter, K.; Petzold, A.; Henze, T.; Thurn-Albrecht, T. Quantitative Analysis of Scanning Force Microscopy Data Using Harmonic Models. *Macromolecules* **2009**, *42*, 1114−1124.

(33) Kim, S.; Misner, M.; Russell, T. Controlling Orientation and Order in Block Copolymer Thin Films. *Adv. Mater.* **2008**, *20*, 4851−4856.

(34) Fasolka, M.; Mayes, A. Block Copolymer Thin Films: Physics and Applications. *Annu. Rev. Mater. Res.* **2001**, *31*, 323−355.

(35) Müller-Buschbaum, P. In *Polymer Surfaces and Interfaces: Characterization, Modification and Applications*; Stamm, M., Ed.; Springer-Verlag: Berlin, 2008.

(36) Scharsich, C.; Lohwasser, R.; Sommer, M.; Asawapirom, U.; Scherf, U.; Thelakkat, M.; Neher, D.; Khler, A. Control of Aggregate Formation in Poly(3-hexylthiophene) by Solvent, Molecular weight, and Synthetic Method. *J. Polym. Sci., Part B: Polym. Phys.* **2012**, *50*, 442−453.

(37) Spano, F. C. Modeling Disorder in Polymer Aggregates: The Optical Spectroscopy of Regioregular Poly(3-hexylthiophene) Thin Films. *J. Chem. Phys.* **2005**, *122*, 234701(01−15).

(38) Murgatroyd, P. Theory of Space-Charge-Limited Current Enhanced by Frenkel Effect. *J. Phys. D: Appl. Phys.* **1970**, *3*, 151−156.

(39) Koster, L. Charge Carrier Mobility in Disordered Organic Blends for Photovoltaics. *Phys. Rev. B* **2010**, *81*, No.205318.

(40) Mihailetchi, V.; van Duren, J.; Blom, P.; Hummelen, J.; Janssen, R.; Kroon, J.; Rispens, M.; Verhees, W.; Wienk, M. Electron Transport in a Methanofullerene. *Adv. Funct. Mater.* **2003**, *13*, 43−46.

(41) Singh, C.; Gupta, G.; Lohwasser, R.; Engmann, S.; Balko, J.; Thelakkat, M.; Thurn-Albrecht, T.; Hoppe, H. Correlation of Charge Transport with Structural Order in Highly Ordered Melt-Crystallized Poly(3-hexylthiophene) Thin Films. *J. Polym. Sci., Part B: Polym. Phys.* **2013**, *51*, 943−951.

(42) Groves, C.; Koster, L. J. A.; Greenham, N. C. The Effect of Morphology upon Mobility: Implications for Bulk Heterojunction Solar Cells with Nonuniform Blend Morphology. *J. Appl. Phys.* **2009**, *105*, 094510(1−6).

(43) Singh, C. R.; Sommer, M.; Himmerlich, M.; Wicklein, A.; Krischok, S.; Thelakkat, M.; Hoppe, H. Morphology controlled open circuit voltage in polymer solar cells. *Phys. Status Solidi RRL* **2011**, *5*, 247−249.